Quantifying the differences in transmission and emission spectra for hot irradiated gaseous exoplanet Atmospheres: A comparison of 1D and 3D modeling using JWST

Rahul Arora, 1,2, Liton Majumdar, 1,2*

¹Exoplanets and Planetary Formation Group, School of Earth and Planetary Sciences, National Institute of Science Education and Research, Jatni 752050, Odisha, India

Accepted XXX. Received YYY; in original form ZZZ

ABSTRACT

Modeling the atmospheres of exoplanets is fundamental to understanding their atmospheric physics and chemical processes. While one-dimensional (1D) atmospheric models with 1D radiative transfer (RT) have been widely used, advances in three-dimensional (3D) general circulation models (GCMs) and 3D RT methods now allow quantitative comparisons of these approaches. With the precision and sensitivity of JWST, such differences can be observationally tested. This study investigates the spectral variations produced by 1D and 3D models and estimates the JWST observing time or number of transits needed to distinguish them. Using HD 189733b as a case study, three sets of simulations were performed: 1D atmospheric models with 1D RT and 3D GCM models coupled with both 1D and 3D RT. An inherent limitation of our study is that the temperature–pressure (T–P) profiles derived from the 3D GCM extend only to the high-pressure regions. The simulations incorporated both equilibrium and disequilibrium chemistry. Significant spectral discrepancies were found, with 3D models generally showing weaker features. Using a JWST noise simulator, the signal-to-noise ratio (SNR) for detecting these differences was calculated. For transmission spectra, the SNR ranged from 2.04–7.68 (equilibrium) and 1.66–7.04 (disequilibrium), while for emission spectra it ranged from 5.90–34.52 (equilibrium) and 7.11–36.93 (disequilibrium). To test the limitations of the 3D GCM, we extended the atmosphere to lower pressures using an isothermal T–P profile and found wavelength-dependent variations in both the spectra and the SNR. These results show that JWST can distinguish 1D from 3D model spectra for major molecular features, underscoring the importance of 3D modeling in interpreting exoplanetary atmospheres.

Key words: exoplanets – planets and satellites: atmospheres – planets and satellites: gaseous planets.

1 INTRODUCTION

Since the discovery of the first exoplanet in 1992, a key focus in astrophysics has been the discovery of more exoplanets and the understanding of their atmospheric characteristics (Seager & Deming 2010). The characterization of exoplanetary atmospheres has significantly advanced through the development of atmospheric models (Fortney 2018). These models establish crucial links between the physical and chemical processes occurring on a planet and the observed photons, allowing us to infer the properties of the atmosphere. As a result, they contribute to our understanding of key planetary processes, including temperature and pressure profiles, as well as the specific chemical composition of the atmosphere (Madhusudhan 2019; Fortney et al. 2021). Moreover, atmospheric models play a pivotal role in confirming the presence of key atmospheric gases, such as water vapor, carbon dioxide, methane, and others, by identifying their spectral signatures (Madhusudhan 2019). The ability of these models to constrain the abundance of gases is essential for determining a planet's habitability, evolutionary history, and potential for hosting life (Madhusudhan 2024).

Nowadays, the most widely used atmospheric models for exoplanets are one-dimensional, modeling the physical structure of the exoplanet in the vertical direction. Some of the most commonly used one-dimensional Radiative-Convective Equilibrium (RCE) models in the community include HELIOS (Malik et al. 2017), ATMO (Tremblin et al. 2015b; Phillips et al. 2020), and PICASO 3.0 (Mukherjee et al. 2023). These are accompanied by one-dimensional radiative transfer models such as petitRADTRANS (Mollière et al. 2019), PI-CASO (Batalha et al. 2019), and PHOENIX (Barman et al. 2001). Although these models have been widely used together with several JWST space-based observations (with JWST Transiting Exoplanet Community Early Release Science Team et al. (2023) being among the most recent, where multiple such forward models were used), they have a few limitations, such as assuming local thermodynamic equilibrium (LTE) and hydrostatic equilibrium, with the most significant limitation being the assumption of a one-dimensional atmosphere. These models rely on the assumption of horizontal homogeneity of

²Homi Bhabha National Institute, Training School Complex, Anushaktinagar, Mumbai 400094, India

^{*} E-mail: liton@niser.ac.in; dr.liton.majumdar@gmail.com

planetary properties, such as temperature, pressure, and chemical composition, including the volume mixing ratios of all gases.

To overcome the assumptions of one-dimensional models, twodimensional models (vertical and one horizontal direction), such as PLATON (Zhang & Chachan 2019) and ATMO (Tremblin et al. 2015a; Drummond et al. 2016; Goyal et al. 2018), as well as threedimensional models like SPARC/MITgcm (Showman et al. 2009), THOR (Deitrick et al. 2022), Exo-FMS (Lee et al. 2021), and the UK Met Office's model (Mayne et al. 2014), have been developed. These models are primarily derived from existing three-dimensional (3D) General Circulation Models (GCMs) developed for Earth. Specifically, 3D GCMs have been extensively used to model a diverse range of exoplanets, including hot Jupiters such as HD 80606b (Tsai et al. 2023b), HD 189733b (Steinrueck et al. 2023), and WASP-39b (Tsai et al. 2023a), as well as terrestrial planets like TRAPPIST-1c (Quirino et al. 2022) and sub-Neptunes such as K2-18b (Innes & Pierrehumbert 2022). Multiple studies have also analyzed the 3D distribution of atmospheric chemistry, focusing on particular aspects of disequilibrium chemistry (Drummond et al. 2020; Lee et al. 2023; Zamyatina et al. 2023). While these models provide a more comprehensive and higher-dimensional representation of a planet's properties, they are computationally expensive, and it remains extremely challenging to study their dynamical, radiative, and chemical processes self-consistently in 3D (Heng & Showman 2015). This raises the question: Can 3D GCMs provide better constraints on planetary physics and chemistry, such as temperature-pressure profiles and atmospheric compositions, from observed transmission and emission spectra compared to 1D models? Additionally, do the model spectra from 3D GCMs show significant differences when compared to those from 1D models that could be observed by current telescopic facilities like the James Webb Space Telescope (JWST)?

To address this question, we modeled HD 189733b, the closest hot Jupiter to Earth at a distance of 63 light-years, and compared the modeled synthetic spectra derived from the 1D RCE model, HE-LIOS (Malik et al. 2017), and the 3D GCM, THOR (Deitrick et al. 2022), coupled with the 1D radiative transfer code petitRADTRANS (Mollière et al. 2019) and the 3D radiative transfer code gCMCRT (Lee et al. 2022). We employed both equilibrium chemistry, using FASTCHEM (Stock et al. 2022), and disequilibrium chemistry, using VULCAN (Tsai et al. 2021). Our source selection is based on the fact that HD 189733b is one of the most well-studied hot Jupiters, particularly suited for atmospheric characterization due to its large size, low mean molecular weight, and large scale heights. Substantial temperature differences between the day and night sides make it an ideal candidate for studying the effects of 3D GCM modeling as well (Heng & Showman 2015). Observations of its transmission and emission spectra using the Hubble Space Telescope (HST) and ground-based facilities have confirmed the presence of several atoms and molecules, including H₂O (Grillmair et al. 2008; Boucher et al. 2021), CO (de Kok, R.J. et al. 2013), Na (Wyttenbach et al. 2015), HCN (Cabot et al. 2019), and K (Keles et al. 2019). Recently, JWST confirmed the detections of H₂O and CO and identified new molecules, such as CO₂ and H₂S (Fu et al. 2024; Inglis et al. 2024). Additionally, a 3D thermal profile of HD 189733b using Spitzer/IRAC at 8 μ m (de Wit et al. 2012) is also available.

The paper is organized as follows: In Section 2, we describe the procedures used to generate the temperature-pressure profiles of the 1D RCE and 3D GCM models, their coupling with chemical codes, and their integration with radiative transfer codes to model transmission and emission spectra under both equilibrium and disequilibrium conditions. Additionally, we describe the noise calculation using the state-of-the-art noise simulator for JWST, PANDEXO (Batalha et al.

2017). In Section 3, we present the spatial variation of physical quantities, show the temperature-pressure profiles and their differences between the 1D and 3D models, along with the differences in volume mixing ratios of major species in the atmospheres under both equilibrium and disequilibrium conditions, and finally present the model transmission and emission spectra. We also discuss the results from our noise calculation and their potential implications for future JWST observations in understanding the 3D nature of the atmospheres as compared to the 1D case. Finally, in Section 4, we summarize our findings and conclusions.

2 METHODOLOGY

Our methodological pipeline for assessing the quantified differences between various combinations of 1D and 3D modeling frameworks and observable spectra is outlined in Figure 1. In this section, we present a detailed description of the methods followed.

2.1 Physical Structure of HD189733b

HD189733b is the nearest Hot Jupiter to Earth and one of the most extensively studied exoplanets. It has a radius of $1.126\ R_J$ and orbits a K-type star with a radius of $0.805\ R_\odot$ and a temperature of 4875 K (Boyajian et al. 2014). To generate the physical structure of HD189733b, we computed the variation of temperature and the K_{ZZ} coefficient/wind velocities with respect to pressure/height in the atmosphere using both 1D and 3D models.

For the 1D model, we used the self-consistent radiative transfer code HELIOS (Malik et al. 2017), which solves for radiative-convective equilibrium to constrain the temperature-pressure profile in the vertical direction. In contrast, the temperature-pressure (T-P) variation in 3D was modeled using THOR + HELIOS, a General Circulation Model (GCM) (Version 2) with a multiwavelength radiative transfer code (Deitrick et al. 2022). For radiative transfer calculations, both the 1D and 3D GCM models considered H_2O , HCN, CH_4 , CO, CO_2 , NH_3 , and H_2 - H_2 , as well as H_2 -He Collision-Induced Absorption (CIA) as sources of opacities . For our simulation, we used a grid of 104 vertical layers spanning a pressure range from 10^{-8} to 200 bar for the 1D model with HELIOS, and we extended the THOR output to the same pressure range using an isothermal T-P profile to ensure consistency between the 1D and 3D GCM grids obtained from THOR.

Table 1 lists the parameters used in the GCM model, which was run under the assumption of non-hydrostatic equilibrium with the reference base pressure set at 200 bar (Deitrick et al. 2020). The simulation grid was chosen to be an icosahedron with 2562 vertices. The model evolved the planet for 1000 Earth days by solving Euler's equations with a timestep of 30 s and performing radiative transfer calculations every five timesteps (i.e., every 150 s). After a few hundred days, the changes in temperature, pressure, and winds became negligible, and the model converged.

In the case of the 3D model, the wind profile from the GCM simulation is used to calculate K_{ZZ} , following Deitrick et al. (2020). However, in the case of the 1D model, due to a lack of wind information, a parametric profile was used, given by Equation 1, following Tsai et al. (2021):

$$K_{ZZ} = K_{deep} \left(\frac{P_{trans}}{P}\right)^{0.4} \tag{1}$$

where K_{deep} is the eddy diffusion coefficient in the deeper regions

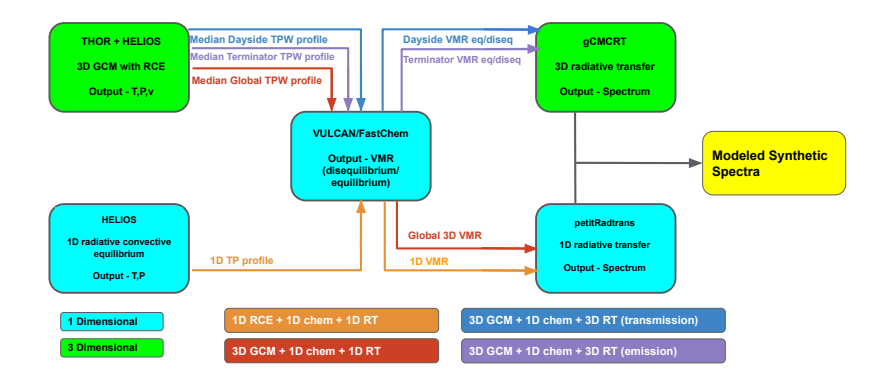


Figure 1. Flowchart illustrating our methodological pipeline, which couples atmospheric, chemical, and radiative transfer codes for each type of simulation. The color codes are as follows: A1 and A2 in orange, B1 and B2 in red, transmission cases C1 and C2 in blue, and emission cases C1 and C2 in light purple. These cases are discussed in Table 4.

Table 1. Input parameters used to simulate the 3D atmosphere of HD189733b using the THOR GCM.

Parameters	Value
Timestep	30 s
Total steps	2,880,000
Radius	786,498,750 m
Rotation rate	$3.28 \times 10^{-5} \text{ rad/s}$
Gravitation	21.5 m/s^2
Gas constant	3516.1 J/(kg K)
Specific heat capacities	12,500 J/(kg K)
Mean temperature	1162 K
Reference pressure	200 bar
Top altitude	3,000,000 m
GCM grid subdivision	4
Vertical layers	53
Stellar temperature	4875 K
Star-planet distance	0.03142 au
Stellar radius	$0.805~R_{\odot}$
Radiative transfer step	2

of the planet, P_{trans} is the transition pressure level, and P is the pressure of the layer.

2.2 Chemical Variation and Observable Spectrum

We studied the chemical variation of HD189733b under equilibrium conditions using FASTCHEM, a gas-phase equilibrium chemistry solver (Stock et al. 2022), and under disequilibrium conditions using VULCAN, a Python-based chemical kinetics code (Tsai et al. 2021) (Table 2). We used solar abundances (Asplund et al. 2009) as the initial elemental abundances for both cases. For disequilibrium chemistry, we employed the NCHO network, which comprises 877 reactions and spans 69 molecules. In disequilibrium chemistry, we included molecular diffusion, eddy diffusion (K_{ZZ}), and photochemical processes. Throughout these simulations, we considered solar metallicity and a C/O ratio analogous to Lee et al. (2023), where they introduced a reduced chemical network code, Mini-chem, and simultaneously modeled HD189733b in 3D.

For modeling the observable transmission and emission spectra, we used a Python-based 1D radiative transfer code, petitRAD-TRANS (Mollière et al. 2019), and a 3D Monte Carlo radiative transfer code, gCMCRT (Lee et al. 2022). For both models, we

Table 2. Parameters used for atmospheric and chemical simulations using 1D and 3D models for disequilibrium conditions. Column 2 represents the 1D radiative-convective equilibrium, and Column 3 represents the 3D general circulation model.

Parameter	1D RCE	3D GCM
$R_{star} (R_{sun})$	0.751	0.751
R_P (cm)	7864987500	7864987500
Gravity (cm/s ²)	2150	2150
Orbit Radius (Au)	0.03142	0.03142
nz (Number of layers)	101	53
P _b (Bottom pressure)	200 bar	GCM T-P profile
P_t (Top pressure)	10^{-6} bar	GCM T-P profile
K_{deep}	$108 \text{ m}^2/\text{s}$	GCM wind profile
P_{trans}	5 bar	GCM wind profile
Initial condition	Equilibrium	Equilibrium

used H_2O , HCN, CH_4 , CO, CO_2 , NH_3 , C_2H_2 , and NO species as sources of opacities. Additionally, HD189733b, being a gas giant, is expected to have an H_2 -He-based bulk atmosphere, which necessitates the inclusion of collision-induced absorption (CIA) due to H_2 -H₂ and H_2 -He. We used correlated-k opacities supplied with the petitRADTRANS package, calculated at R=1000, and the same opacities were used in the 3D radiative transfer code gCMCRT.

For gCMCRT, we used a 3D grid of 45 latitude points, 90 longitude points, and 53 vertical layers, simulated by THOR. We applied transit chord ray tracing and g-ordinance biasing for the transmission spectrum. gCMCRT uses the convention of the substellar point being at 90° latitude (given by the parameter ϕ) and 0° longitude (given by the parameter θ). The observer for transmission was set at 90° ϕ and 180° θ , which corresponds to the antistellar point. For the emission spectrum, the observer was set at 90° ϕ and 0° θ , which is the substellar point. Other parameters are shown in Table 3.

2.3 Modeling HD 189733b in 3D and 1D

To study an exoplanet in 3D, we lack a 3D disequilibrium chemistry solver. For 3D modeling, we consider two cases: one with a 3D GCM and a 1D chemical profile with 1D radiative transfer, and a second with a 3D GCM, a 1D chemical profile, and 3D radiative transfer. In the first case, we take the global median of the T-P profile calculated at different latitudes and longitudes. This 1D global median profile is then used to calculate the vertical volume mixing ratios (VMRs)

Table 3. Table showing the parameters used to calculate opacity (Columns 1 and 2) and the simulation parameters for 3D radiative transfer (Columns 3 and 4) used in gCMCRT.

Opacity parameters		Radiative transfer parameters	
Correlated-K		Transmission limb sampling	True
Pre-mixed opacity	False	g-ordinance bias	True
Wavelength interpolation	False	Number of photons	102400
		Wavelength points	5115
Number of g ordinances	16	Number of theta points	46
CIA		Number of phi points	91
		Viewing theta (degrees)	90
		Viewing phi (degrees)	180, 0

Table 4. Nomenclature of different model simulations

Model Code	Atmospheric Structure	Radiative Transfer	Chemical Conditions
A1	1D	1D	Equilibrium
A2	1D	1D	Disequilibrium
B1	3D	1D	Equilibrium
B2	3D	1D	Disequilibrium
C1	3D	3D	Equilibrium
C2	3D	3D	Disequilibrium

of molecules in both equilibrium and disequilibrium. Both the 1D VMR profile and the global median profile are used to perform 1D radiative transfer.

For the second case, we divide the process into two sections: the transmission spectrum and the emission spectrum. For the transmission spectrum, we use the median profile of the east and west terminators to calculate the VMRs of molecules, generating spectra for both east and west terminator profiles by performing 3D radiative transfer. The final transmission spectrum is the average of the spectra from both terminators. For the emission spectrum, we take the median T-P profile of the dayside of the planet and repeat the method used for the transmission spectrum to obtain the emission spectrum. Both processes are performed for equilibrium and disequilibrium chemistry.

In the above method, we use the median instead of the mean to convert the 3D Temperature-Pressure-Wind (T-P-W) distribution to 1D. This is because the minimum pressure on the planet's dayside and nightside differ by two orders of magnitude. The mean average pressure cannot represent the correct distribution of pressure levels. To address this, we use the median of all quantities.

For the case of a 1D study of the atmosphere, we model the 1D T-P profile, calculate the K_{ZZ} using Equation 1, and determine the VMR in both equilibrium and disequilibrium conditions. Using the calculated VMR, we perform 1D radiative transfer to generate the model spectrum. A nomenclature of these models is shown in Table 4.

2.4 Noise Simulation and SNR calculation

Once the synthetic spectra are generated, we simulate JWST observations using PANDEXO (Batalha et al. 2017) to quantify the differences in observability between models A1, A2, B1, B2, C1, and C2. Using PANDEXO, we simulate NIRSpec (Near Infrared Spectrograph) and MIRI (Mid Infrared Spectrograph) observations covering the wavelength ranges of 0.7–5 μ m and 5–14 μ m, respectively. For NIRSpec, we simulate observations with three grisms: G140M (0.7–1.89 μ m), G235M (1.7–3 μ m), and G395M (2.9–5 μ m), covering the full range of NIRSpec wavelengths. For MIRI, we

include the MIRI MRS instrument (5–14 μ m). We run noise simulations for each transit, which lasts 1.8 hours, and add 2 hours of baseline observation, totaling 3.8 hours. The stellar parameters used for the noise simulation are shown in Table 5. PANDEXO uses these parameters to generate stellar fluxes using PHOENIX models. All these instruments share the same spectral resolution of 1000 in our simulation, consistent with our modeled spectra. An additional floor noise of 14 ppm is added for all simulations.

We adopt the methodology described in Lustig-Yaeger et al. (2019) for the SNR calculation. The absolute difference between the 3D and 1D spectra, at which the noise is calculated, is determined first. Then, additional noise is computed using Equation 2 to account for the out-of-transit baseline noise, as explained in Fauchez et al. (2022).

$$N_{baseline} = \sqrt{\left(\frac{1}{t_{out}}\right)^2 + \left(\frac{1}{t_{in}}\right)^2} \tag{2}$$

The signal-to-noise ratio at each wavelength point, $\left(\frac{S}{N}\right)_i$, is calculated using Equation 3:

$$\left(\frac{S}{N}\right)_{i} = \frac{\Delta f}{N_{baseline} \cdot N_{Pandexo}} \tag{3}$$

where Δf is the difference in transit depth or flux ratio between the 3D and 1D models, $N_{baseline}$ is the baseline noise calculated using Equation 2, and $N_{Pandexo}$ is the simulated noise from PANDEXO.

Using the JWST noise simulated with PANDEXO, we calculate the signal-to-noise ratio (SNR) achievable with the observation of one transit of HD189763b using Equation 3. We then use Equation 4 to calculate the SNR achieved in N_T transits.

$$\left(\frac{S}{N}\right)_{T} = \sqrt{N_T \cdot \left(\frac{S}{N}\right)_{i}^2} \tag{4}$$

Table 5. Stellar parameters used for PANDEXO simulation

Parameter	Value
Magnitude (J band) ^b	6.07
Temperature ^a	5052 K
Reference wavelength (J band)	1.25 μ m
Metallicity ^a	-0.02
Surface gravity (log) ^a	4.49

The above parameters have been sourced from the following sources: a: Exomast, b: SIMBAD

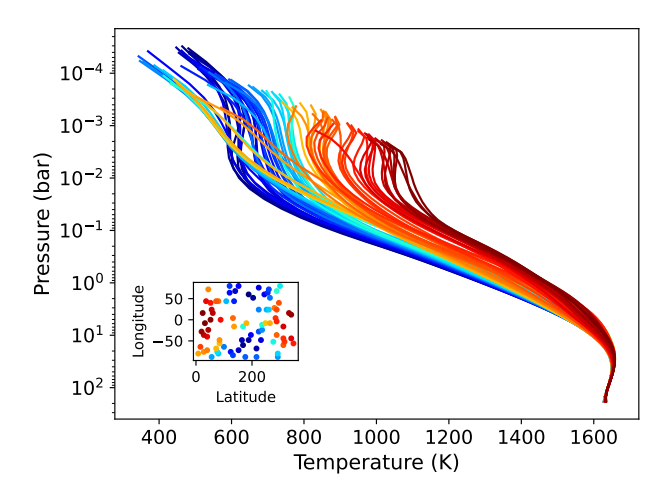


Figure 2. Comparison of T-P profiles at different latitudes and longitudes of the planet. The subplot shows the color coding of the T-P profiles with respect to latitude and longitude. The point (0,0) corresponds to the substellar point.

3 RESULTS AND DISCUSSIONS

In this section, we examine the quantitative differences between the modeled transmission and emission spectra of HD189733 b using 1D and 3D modeling techniques. We particularly highlight the importance of 3D General Circulation Models (GCMs) for accurately representing the physical characteristics of the planet and the effects of 3D radiative transfer, in contrast to 1D radiative transfer. We discuss our results under both equilibrium and disequilibrium conditions.

3.1 Spatial variation of physical quantities in HD189733b

We evolved the HD189733b planet for 1000 Earth days using THOR GCM, starting with a uniform distribution of the Guillot T-P profile (Guillot 2010). After the planet's physical processes converged, a distribution of T-P profiles was obtained, as shown in Figure 2. We observed an increasing variation in pressure and temperature in different parts of the planet with height.

We observed that wind velocities directly impact the movement of material and, consequently, the redistribution of heat. In the lower region of the atmosphere, wind velocities are very small due to the high mass density, which makes the redistribution of material and heat inefficient, leading to a homogeneous temperature distribution, as shown in Figure 3. In contrast, in the upper regions of the atmosphere, high wind velocities enable efficient redistribution of heat, as can be seen in Figure 4.

The temperature distribution of the planet showed an eastward

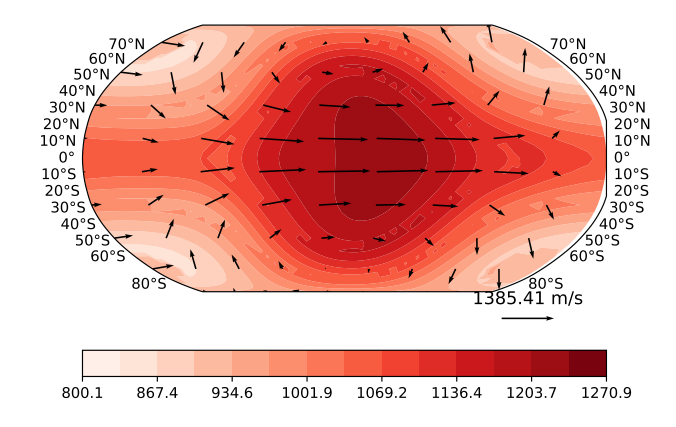


Figure 3. Horizontal distribution of temperature on the planet at a pressure level of 0.1 bar. Arrows represent the wind speed and direction at every 10° latitude and longitude point, relative to the THOR grid system.

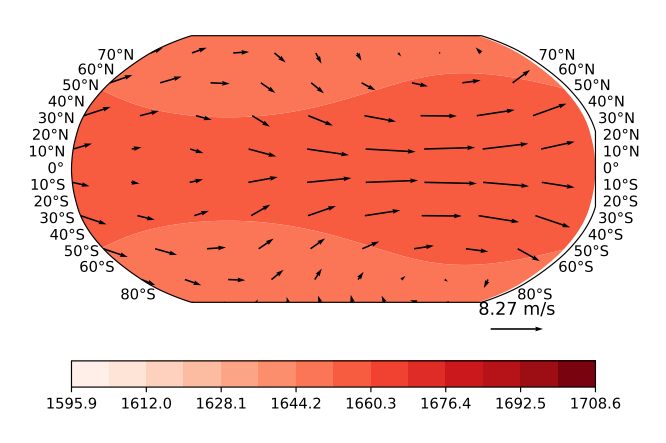


Figure 4. Same as Figure 3, but at a pressure level of 30 bar.

shift of $16^{\circ} \pm 4^{\circ}$ in the planet's hotspot, due to the wind movement in the eastward direction caused by the planet's rotation from west to east. This eastward shift is also observed in Spitzer and HST data, as reported by de Wit, J. et al. (2012) and Pont et al. (2013).

3.2 Comparison of T-P profiles computed using 1D and 3D models

In our comparison, we generated a 1D T-P profile in radiative-convective equilibrium using HELIOS and a 3D T-P profile using the THOR GCM. For the 1D profile, we used a parametric profile for the eddy diffusion coefficient, as given by Equation 1, with K_{deep} set to $10^8~\rm cm^2 s^{-1}$ and P_{tran} set to 5 bar. For the 3D GCM, the eddy diffusion coefficient profile was calculated using the wind profile obtained from the GCM output. Figure 5 shows the comparison between the 1D profile, the median global average 3D profile, the

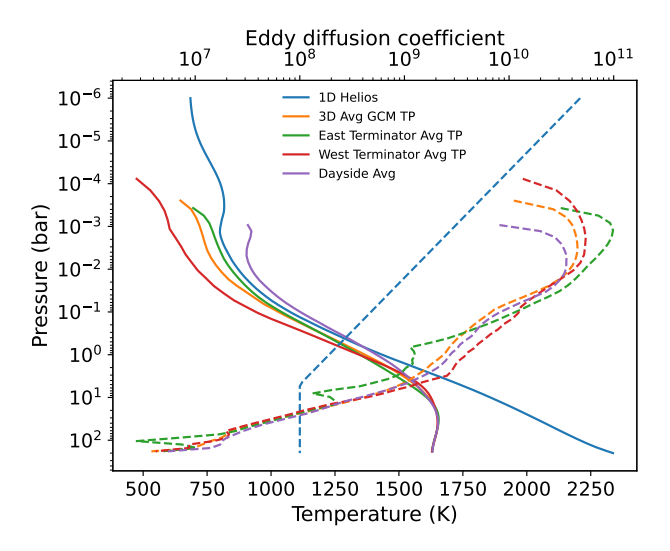


Figure 5. This figure compares the 1D radiative-convective equilibrium profile (solid blue) with the median globally averaged 3D temperature-pressure (T-P) profile (solid orange), the median east terminator average (solid green), the median west terminator average (solid red), and the median dayside average (solid purple). The dashed lines represent the eddy diffusion coefficient (K_{ZZ}) for each respective case.

median east terminator average, the median west terminator average, and median dayside average T-P and K_{ZZ} -P profiles.

For the 1D T-P profile, we observe that the temperature is slightly higher than that of the median average T-P profile obtained from the 3D GCM. This overall shift is due to the fact that the 1D radiativeconvective equilibrium assumes irradiation perpendicular to the vertical grid, while in the case of the 3D GCM, direct irradiation only affects the planet's dayside. This results in the night side being cooler, leading to a lower median average global temperature for the planet. Additionally, in the lower regions of the planet (higher pressure regions), the temperature exhibits a monotonically increasing trend in the 1D profile, whereas an isothermal nature is observed for the 3D GCM. As shown in Figures 3 and 4, high-pressure regions have very low horizontal wind velocity, making heat redistribution inefficient. In contrast, effective heat redistribution occurs in the low-pressure regions, preventing much stellar heat from being transferred into the lower regions of the planet, resulting in an isothermal profile. Due to wind movement from west to east, the eastern terminator (90° longitude, latitude ranging from $0^{\circ} - 90^{\circ}$) is hotter than the western terminator (270° longitude, latitude ranging from $0^{\circ} - 90^{\circ}$).

3.3 T-P profile extension to photochemical layers

THOR is an altitude-based GCM model that does not converge at pressures lower than 10^{-4} bar (Deitrick et al. 2022). This limitation excludes an important atmospheric region where photochemical processes are highly active. To incorporate this region, we recalculated the 1D T–P and K_{ZZ} profiles with a top-of-atmosphere pressure of 10^{-8} bar and extended the temperature and K_{ZZ} profiles of all 3D models down to 10^{-8} bar using isothermal extrapolation, ensuring consistency with the 1D profiles. Figure 6 compares the 1D radiative–convective equilibrium profile with the median global average 3D profile, the median east terminator average, the median west terminator average, and the median dayside average T–P and K_{ZZ} –P profiles, all extended from 10^{-4} to 10^{-8} bar under isothermal conditions.

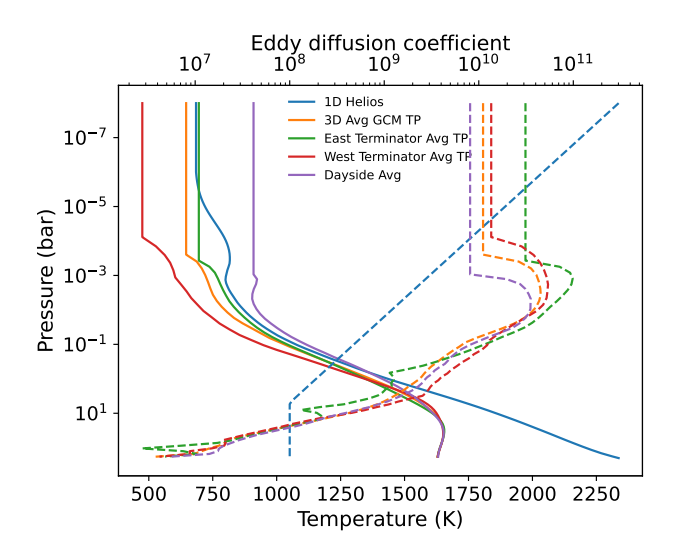


Figure 6. T–P profiles, similar to those in Figure 5, are shown for an extended atmosphere ranging from 10^{-4} to 10^{-8} bar under isothermal conditions for all 3D cases.

3.4 Variation of atmospheric volume mixing ratios across different physical structure cases

We calculated the volume mixing ratios (VMRs) for five temperature–pressure–wind (T–P–W) profiles under both equilibrium and disequilibrium conditions. These five T–P–W profiles are: the 1D radiative–convective equilibrium profile (1D RCE) with a parametric K_{ZZ} profile, the median global average profile (GA), the median east terminator average profile (ETA), the median west terminator average profile (WTA), and the median dayside average profile (DA). Figure 5 shows these T–P profiles, while all 3D cases extended up to 10^{-8} bar under isothermal conditions, along with the 1D self-consistent case where the top of the atmosphere is set to 10^{-8} bar, are shown in Figure 6. Figure 7 illustrates the vertical profiles of the volume mixing ratios for six major opacity sources corresponding to the non-extended T–P profiles, whereas Figure 8 presents the same for the extended T–P profiles.

Lower and Middle Atmosphere

We observe that the VMR profiles of ETA and 1D RCE are largely similar due to their comparable T-P profiles, as shown in Figure 5. The ETA and 1D RCE cases, having higher temperatures, exhibit higher abundances for all gases except HCN and CO in the upper parts of the atmosphere (< 0.1 bar). We also find that $\rm H_2O$ and CO exhibit different abundances between the 1D RCE and both ETA in the 3D model, as shown in Figures 7A and 7B. This difference is primarily observed in the lower regions of the atmosphere (100–10 bar), where equilibrium chemistry dominates. A similar trend is observed for the other four molecules in this region.

For the disequilibrium case shown in Figure 7B, we found the following trends. In both the east terminator average (ETA) and west terminator average (WTA) 3D models, HCN abundances in the middle atmosphere (0.1–10⁻⁵ bar) are regulated by a balance between formation through $H_2 + CN \rightarrow H + HCN$ and destruction via the three-body pathway HCN + H + M \rightarrow H₂CN + M. These reactions proceed in both directions and dominate across both limbs, maintaining moderate HCN levels through reversible hydrogenation and radical cycling. In the 1D radiative-convective equilibrium (RCE)

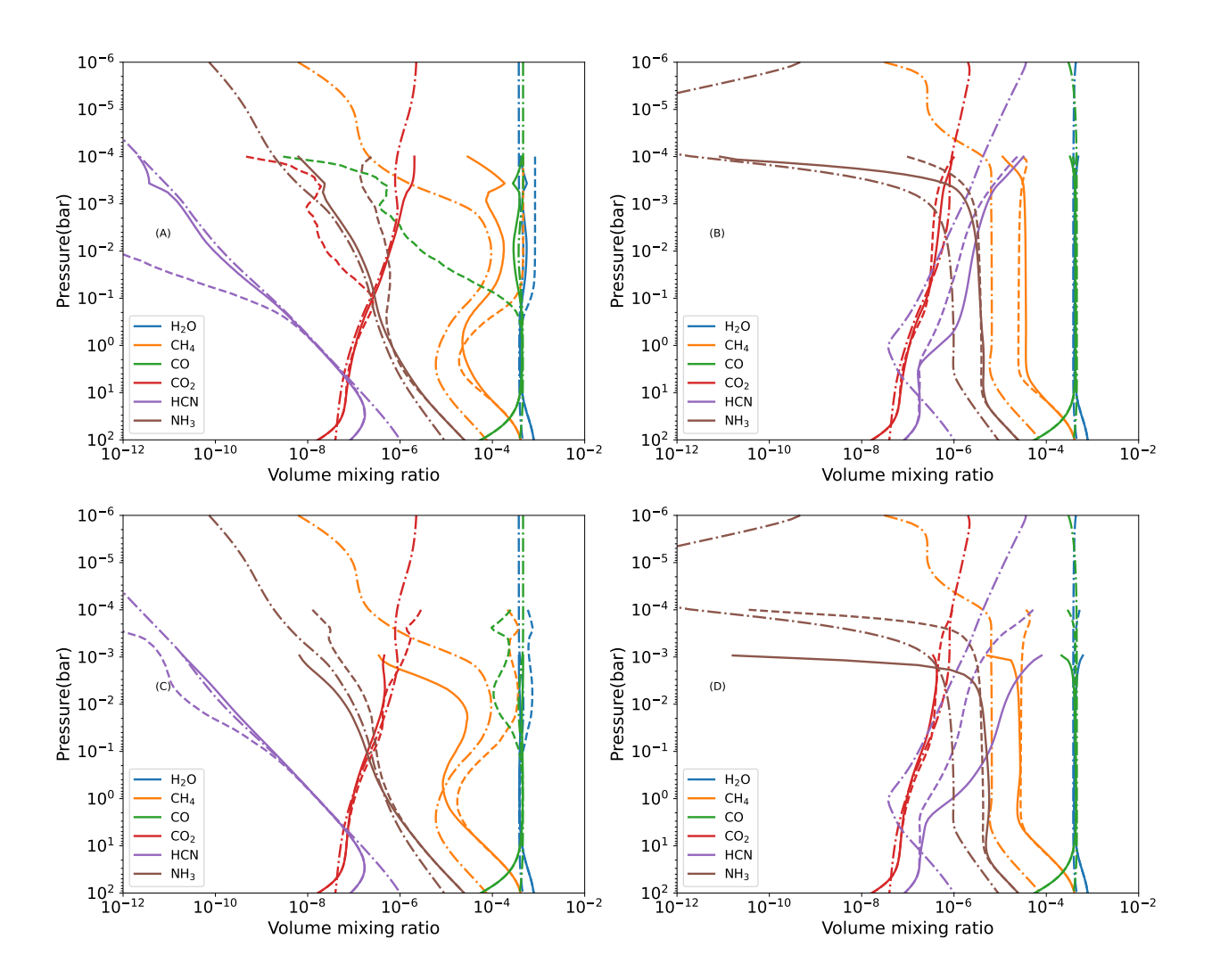


Figure 7. Vertical profiles of the volume mixing ratios for six major opacity sources under chemical equilibrium and disequilibrium conditions, calculated using the T-P and K_{ZZ} -P profiles shown in Figure 5. Each subfigure presents results for three different temperature-pressure profiles. The first column (Panels A and C) shows equilibrium chemistry models, while the second column (Panels B and D) presents disequilibrium models. In Panels (A) and (B), the three models correspond to the median east-side terminator average from the 3D GCM (solid line), the median west-side terminator average from the 3D GCM (hashed line), and the 1D radiative-convective equilibrium model (hashed + dotted line). In Panels (C) and (D), the three models represent the median dayside average from the 3D GCM (solid line), the median global terminator average from the 3D GCM (hashed line), and the 1D radiative-convective equilibrium model (hashed + dotted line).

model, however, the reaction $H_2CN + H \rightarrow HCN + H_2$ also contributes significantly to HCN formation. Nevertheless, HCN destruction via HCN + H + M \rightarrow H₂CN + M occurs at a relatively higher rate in the 1D model than in the terminator models, resulting in a net decrease in HCN abundances at comparable pressures.

In both the ETA and WTA 3D models, NH_3 formation in the middle atmosphere $(0.1-10^{-5} \text{ bar})$ is dominated by $NH_2 + H_2 \rightarrow NH_3 + H$. The reversible nature of this pathway, together with direct thermal decomposition of NH_3 into $NH_2 + H$, establishes a dynamic equilibrium that governs local NH_3 levels. An additional production

channel, NH₂ + CH₄ \rightarrow CH₃ + NH₃, is also active on both limbs, highlighting the role of hydrocarbon chemistry in nitrogen coupling. In the 1D RCE model, NH₃ formation is primarily driven by NH₂ + H₂ \rightarrow NH₃ + H and the three-body reaction H + NH₂ + M \rightarrow NH₃ + M, reflecting more efficient recombination under smoother vertical gradients and higher pressures.

In all three models, CH_4 formation in the middle atmosphere $(0.1-10^{-5} \text{ bar})$ is dominated by $H + CH_3 + M \rightarrow CH_4 + M$, while destruction occurs via $H + CH_4 \rightarrow CH_3 + H_2$ and its reverse. In the ETA and WTA models, CH_4 is also destroyed through oxidation by

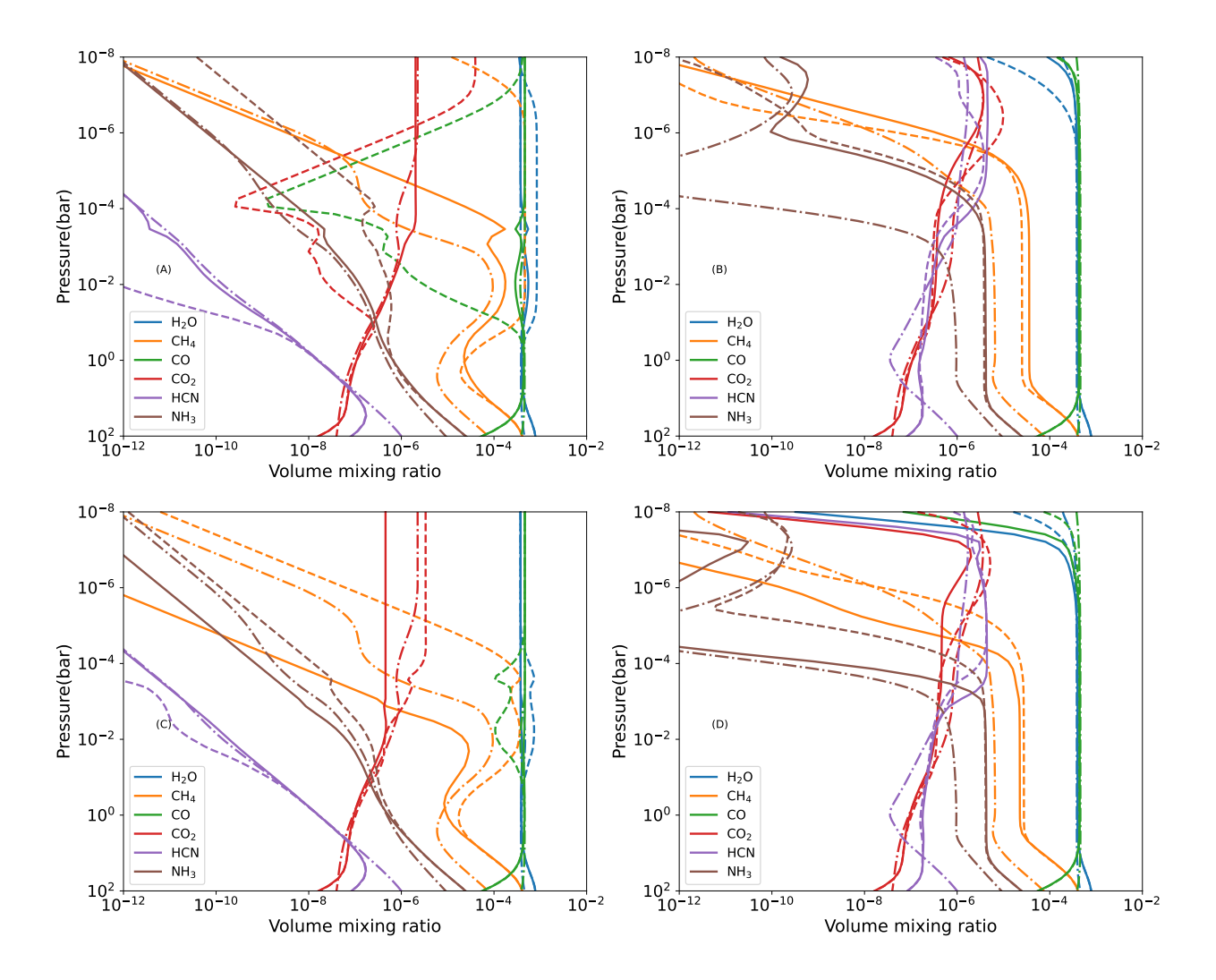


Figure 8. Vertical profiles of the volume mixing ratios for six major opacity sources under chemical equilibrium and disequilibrium conditions, calculated using the T-P and K_{ZZ} -P profiles shown in Figure 6. Each subfigure presents results for three different temperature-pressure profiles. The first column (Panels A and C) shows equilibrium chemistry models, while the second column (Panels B and D) presents disequilibrium models. In Panels (A) and (B), the three models correspond to the median east-side terminator average from the 3D GCM (solid line), the median west-side terminator average from the 3D GCM (hashed line), and the 1D radiative-convective equilibrium model (hashed + dotted line). In Panels (C) and (D), the three models represent the median dayside average from the 3D GCM (solid line), the median global terminator average from the 3D GCM (hashed line), and the 1D radiative-convective equilibrium model (hashed + dotted line).

OH via OH + CH₄ \rightarrow H₂O + CH₃, which is absent in the 1D RCE model. This difference leads to more efficient CH₄ depletion in the 3D models compared to the 1D case, where CH₄ remains relatively more stable due to fewer loss pathways.

At high pressures and temperatures, the chemical timescale becomes shorter than the eddy diffusion timescale, resulting in molecular abundances governed by equilibrium chemistry. This behavior is evident in Figure 7, where panels (A) and (B) show similar molecular abundances for the western and eastern terminators under both

equilibrium and disequilibrium chemistry in the pressure range of $200\ \mathrm{to}\ 10\ \mathrm{bar}.$

In both the dayside-average and global-terminator-average 3D models, HCN abundances in the middle atmosphere $(0.1-10^{-5} \text{ bar})$ are governed by the same bidirectional reactions as in the terminator models shown in subplot B, namely $H_2 + CN \rightleftharpoons H + HCN$ and HCN $+ H + M \rightleftharpoons H_2CN + M$. The global terminator model in subplot D shows chemical behavior nearly identical to that of the west terminator in subplot B, with all four reactions active and balanced. The 1D RCE model also retains the same pathways as in subplot B, indi-

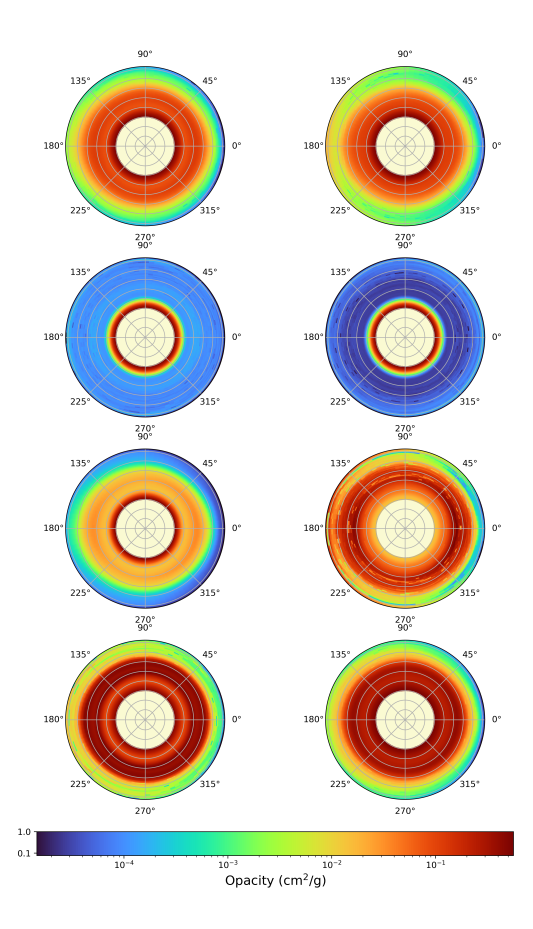


Figure 9. Polar maps of the total mass opacity used in the 3D radiative-transfer simulations. Each panel shows the spatial distribution of opacity across latitude and longitude, computed using equilibrium-chemistry opacities for the full 3D temperature structure. The eight subpanels correspond to opacity fields at eight wavelength points (1.28 μ m, 1.54 μ m, 2.24 μ m, 2.28 μ m, 3.2 μ m, 4.32 μ m, 7.71 μ m, and 9.95 μ m), illustrating how the wavelength and temperature dependence of line and continuum features maps onto spatial dependence in the atmosphere. The color scale shows the total mass opacity (cm² g⁻¹) on a logarithmic scale.

cating broadly consistent chemistry within this pressure range across all viewing geometries.

In subplot D, the middle-atmospheric chemistry of NH $_3$ closely parallels that in subplot B, with NH $_2$ + H $_2 \rightleftharpoons$ NH $_3$ + H dominating across all models. The dayside model includes an additional oxidation-driven loss via the reverse of NH $_3$ + OH \rightarrow NH $_2$ + H $_2$ O, similar to the west terminator in subplot B. The global terminator and 1D models show nearly identical behavior to the 1D RCE model in subplot B, relying on NH $_2$ + H $_2 \rightleftharpoons$ NH $_3$ + H and the three-body recombination reaction H + NH $_2$ + M \rightarrow NH $_3$ + M for NH $_3$ formation.

In subplot D, CH₄ abundances in the middle atmosphere $(0.1-10^{-5}$ bar) are regulated by the same hydrogen-abstraction and recombination reactions as in subplot B, namely H + CH₄ \rightleftharpoons CH₃ + H₂ and H + CH₃ + M \rightarrow CH₄ + M. In the dayside model, CH₄ destruction is

enhanced by OH + CH $_4$ \rightarrow H $_2$ O + CH $_3$, reflecting chemical behavior similar to that observed at the east terminator in subplot B. The global terminator model also includes this oxidation pathway, while the 1D model retains only the core abstraction and OH reactions, consistent with subplot B.

Similarly, Figure 7 (C) presents three equilibrium VMR profiles derived from the T-P-W profiles of 1D RCE (hashed + dotted line), DA (solid line), and GA (hashed line), while Figure 7 (D) shows the corresponding disequilibrium VMR profiles. The DA profile provides the best representation of the chemical composition that would be imprinted on the emission spectra as the emission spectra are generated on the dayside of the planet just before the secondary eclipse. We observe similar trends for DA and GA in the case of H_2O , CO, and CO_2 , as seen in ETA and WTA (Figure 7 A and C). All three models shown in Figure 7 (D) share a common major formation pathway, characterized by the dissociation of CN by H_2 : $H_2 + CN \rightarrow H + HCN$. Despite having the same formation pathway, the reaction rates differ by several orders of magnitude across the three cases in the atmosphere above 1 bar, leading to significant variations in HCN abundance.

Comparing the 1D RCE and DA profiles, we find similarities in their T-P profiles and equilibrium VMR profiles. The equilibrium abundances of gases show a direct correlation with temperature and pressure variations, which explains the similar VMR profiles observed in these two cases. Under disequilibrium conditions, the dayside profile exhibits behavior similar to that of the east and west terminator profiles due to small differences in the T-P and K_{zz} profiles of these models.

Extended Upper Atmosphere

In the upper atmosphere (pressures < 0.1 bar), where the transmission technique is most sensitive, the models predict an order-of-magnitude decrease in the abundances obtained from the 1D RCE model in Figure 8A compared to those calculated for the terminator region (WTA), particularly for CH₄, HCN, and NH₃.

In the upper atmosphere ($<10^{-5}$ bar), photodissociation of HCN via HCN + h ν \rightarrow H + CN becomes significant in both the ETA and WTA models, contributing to HCN depletion. However, concurrent recycling pathways such as H₂ + CN \rightarrow H + HCN and H₂CN + H \rightarrow HCN + H₂ help sustain HCN at low pressures, particularly on the east limb. In contrast, the 1D RCE model, which lacks explicit photochemical loss terms, maintains HCN primarily through hydrogenation and CN recombination, likely leading to an overestimation of HCN abundance in this region.

 NH_3 is photodissociated through $NH_3 + h\nu \rightarrow NH_2 + H$ in all three models. Despite this loss, NH_3 is partially replenished through $NH_2 + H_2 \rightarrow NH_3 + H$, though the efficiency of this recycling varies. On the west limb, minor contributions arise from the reverse reaction $NH_3 + CH \rightarrow NH_2 + CH_2$, while in the 1D model, the reverse of $NH_3 + OH \rightarrow NH_2 + H_2O$ also plays a role. The net result is a decline in NH_3 abundance with altitude in all models, although the magnitude of depletion differs due to the interplay between photochemistry and vertical mixing. The substantial variation in NH_3 abundances can be attributed to an order-of-magnitude difference in formation rates, likely caused by a high K_{ZZ} value, which leads to shorter kinetic and longer chemical timescales, thereby reducing reaction efficiencies.

 CH_4 undergoes photodissociation in the 3D models through CH_4 + $h\nu \rightarrow CH_2$ + H_2 , while also participating in reversible hydrogen abstraction and recombination (H + CH_3 + M \rightarrow CH_4 + M). These processes counteract each other, with photolysis driving CH_4 loss and radical chemistry partially restoring it. In contrast, the 1D model lacks

photodissociation and maintains higher CH_4 levels, with destruction occurring mainly through $H + CH_4 \rightarrow CH_3 + H_2$ and oxidation by OH. This leads to an overprediction of CH_4 abundance at low pressures in the 1D framework.

Photodissociation of HCN via HCN + $h\nu \rightarrow CN + H$ is enhanced in the dayside model, leading to enhanced HCN depletion compared to both the global terminator and 1D models. The latter two rely solely on the reversible $H_2 + CN \rightleftharpoons H + HCN$ and $HCN + H + M \rightleftharpoons H_2CN + M$ reactions, as in subplot B, resulting in higher HCN abundances at low pressures. The presence of photolytic destruction in the dayside case, partially offset by $H_2CN + H \rightarrow HCN + H_2$, introduces a key divergence from the more shielded regions represented in subplot B.

3.5 Modelled synthetic transmission and emission spectrum

3.5.1 Non-extended Cases

We present four comparison cases in Figure 10. Figure 10A shows the transmission spectra computed under chemical equilibrium for (i) a full 1D model, (ii) a 3D GCM (GA) with 1D chemical profiling and 1D radiative transfer, and (iii) a 3D GCM (ETA and WTA averages) with 1D chemical profiling and 3D radiative transfer and (iv) a 3D GCM (DA) with 1D chemical profiling and 3D radiative transfer, using the T-P profiles shown in Figure 5. Figure 10B presents the same cases but with disequilibrium chemistry. Similarly, Figure 10C shows emission spectra using equilibrium chemistry for (i) a complete 1D model, (ii) a 3D GCM (GA) with 1D chemical profiling and 1D radiative transfer, and (iii) a 3D GCM (DA) with 1D chemical profiling and 3D radiative transfer. Figure 10D presents the same cases but with disequilibrium chemistry. Differences in molecular abundances and the radiative transfer method are the two primary factors contributing to the discrepancies between our 1D and 3D models. We discuss the effects and variations in molecular abundances in Section 3.4. For radiative transfer, we use petitRADTRANS for the 1D model and gCMCRT for the 3D model. Due to differences in their working dimensionality, these models take different temperature-pressure distributions as input. For the 3D simulation, even when using the same volume mixing ratios as the 1D radiative transfer simulation, inhomogeneous opacity is observed, as shown in Figure 9. This demonstrates how, for the same VMR, variations in opacity in the 3D simulations lead to differences in the transmission and emission spectra compared to the 1D radiative transfer model. The opacity plots indicate higher opacity toward the nightside, which corresponds to lower temperatures and pressures, whereas lower opacity is observed on the dayside, where temperatures and pressures are higher. These differences result in an overall decrease in transit depth for the 3D model, as discussed in Section 3.5.2.

3.5.2 Transmission Spectra

We modeled synthetic transmission spectra for three cases, as defined in Section 2.3, using both equilibrium and disequilibrium chemistry. Figures 10 (A) and (B) compare the transmission spectra of the three modeled cases.

In the case of equilibrium chemistry, shown in Figure 10 (A), the differences between the orange and green curves arise solely from variations in the T-P profiles, which affect the 1D equilibrium molecular abundances. In contrast, the differences between the blue and orange curves result from the use of different radiative transfer methods. The 3D radiative transfer (RT) technique underestimates spectral features compared to the 1D RT method. We observe that H₂O, CH₄, CO₂, and CO exhibit the most distinguishable spectral

differences between the 1D and 3D models, with variations exceeding 100 ppm. A more detailed quantitative assessment of the wavelength-dependent signal differences is provided in Table 6.

Figure 10 (B) presents the synthetic transmission spectra for disequilibrium chemistry. We find that the difference in transit depth between the 1D and 3D models decreases for all molecules except for the combined $\rm H_2O$ + $\rm CH_4$ feature in the 2.15–3 μm range.

Furthermore, we identify significant differences between the equilibrium and disequilibrium spectra. All major H_2O features exhibit greater transit depths in equilibrium models compared to disequilibrium models, with differences exceeding 50 ppm in the 1D models and 100 ppm in the 3D models. Equilibrium chemistry also predicts a higher CH_4 abundance than disequilibrium conditions, as CH_4 readily photolyzes into CH_3 and H a process not accounted for in equilibrium chemistry.

3.5.3 Emission Spectra

In our study, the median dayside-averaged profile used for 3D RT is the hottest, followed by the 1D RCE profile, while the global median profile is the coldest. Figures 10 (C) and (D) illustrate these temperature variations. We also find that differences between the emission spectra of the 1D and 3D models are highly wavelength-dependent, with larger deviations at longer wavelengths due to the higher emission flux from the planet at those wavelengths.

Figure 10 (C) shows the synthetic emission spectra under equilibrium chemistry for HD 189733b. In this case, we observe significant differences between the 1D and 3D models (371–1004 ppm), primarily attributed to CH_4 , CO, CO_2 , and NH_3 . Unlike the transmission spectra, the 1D and 3D emission spectra exhibit no notable differences in H_2O signals.

Figure 10 (D) presents the synthetic emission spectra under disequilibrium chemistry. The disparity between the 1D and 3D models decreases under disequilibrium conditions, similar to what we observed for the transmission spectra. As in the equilibrium case, differences of 285–807 ppm arise, mainly due to the same opacity sources (CH₄, CO, CO₂, and NH₃). CH₄ is the most significantly affected opacity source under disequilibrium conditions, as evidenced by the sharp decrease in its 7.4–7.74 μ m and 14 μ m features in Figure 10 (D). The impact of CH₄ photodissociation (Section 3.4) on signal strength is more pronounced in the 3D models, indicating that they are more sensitive to the treatment of chemistry compared to 1D models.

3.5.4 Extended Cases and Limitations

A key limitation of our extended cases arises from the numerical pressure ceiling in THOR, which typically reaches up to 10^{-4} bar (Deitrick et al. 2022). For photochemical modeling, we extrapolated these T–P–W profiles isothermally to 10^{-8} bar to capture photochemical effects. However, since gCMCRT is built on a constant-height grid, extending the grid to 10^{-8} bar on the dayside causes the corresponding nightside levels to fall below 10^{-10} bar, resulting in numerical instabilities. Consequently, we generate spectra for the extended cases only with the 1D radiative transfer model to examine how the extended atmospheres compare with the non-extended cases and to assess the impact of photochemistry. The extended atmospheric spectra are shown in Figure 11 for the 1D RCE + 1D chemistry + 1D RT and 3D GCM + 1D chemistry + 1D RT configurations, alongside the non-extended spectra (3D GCM + 1D chemistry + 3D RT), enabling direct comparison between the extended and non-extended

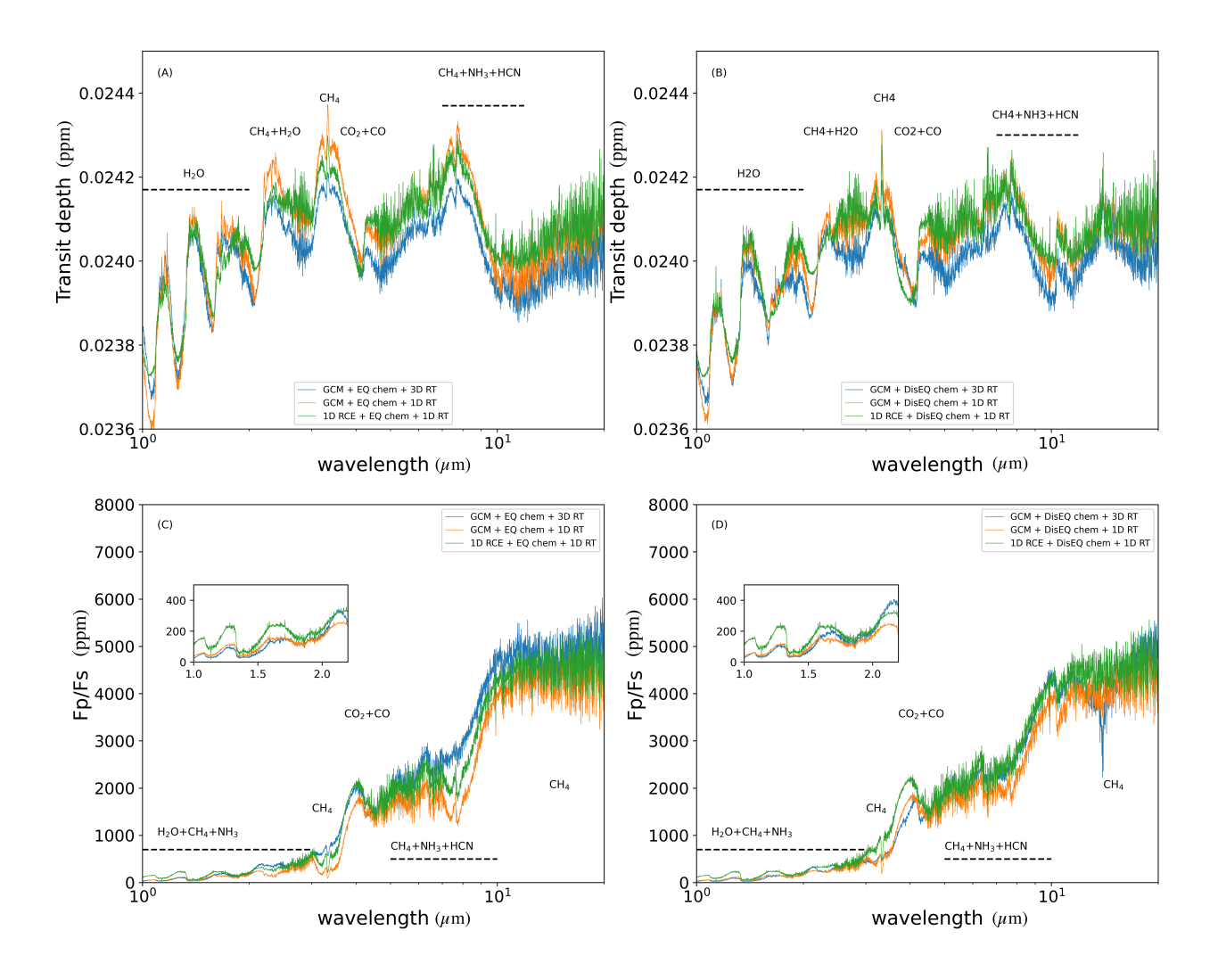


Figure 10. Subfigures (A) and (B) show the transmission spectrum using equilibrium and disequilibrium chemistry, respectively, from the three different cases compared in our study: complete 1D modeling (green), 3D GCM (GA) with 1D chemical profiling and 1D radiative transfer (orange), and 3D GCM (ETA and WTA average) with 1D chemical profiling and 3D radiative transfer (blue) using the T–P profiles shown in Figure 5. Subfigures (C) and (D) represent the emission spectrum using equilibrium and disequilibrium chemistry, respectively, with a color scheme similar to (A) and (B).

cases and illustrating the signal differences listed in Table 6. Comparing the 1D RCE + 1D chemistry + 1D RT with the 3D GCM + 1D chemistry + 1D RT reflects only the differences in the T–P profiles, rather than in the modeling techniques, which are the main focus of this study. Therefore, in Table 6, the extended difference case represents the difference between the extended 1D RCE + 1D chemistry + 1D RT and the non-extended 3D GCM + 1D chemistry + 3D RT. This comparison highlights the impact of the lower-pressure upper atmosphere.

3.5.5 Transmission Spectra

In transmission, the extended 1D–3D comparison shows that the largest contrasts occur in water-dominated regions and in the blended $\rm H_2O+CH_4$ band. Under disequilibrium chemistry, the inclusion of the extended upper atmosphere produces only small changes in most features, with differences varying by less than 20 ppm for $\rm H_2O$ bands and decreasing substantially for $\rm CH_4$ and $\rm CO/CO_2$ regions, in some cases by nearly half. In the equilibrium case, the effect of the extended atmosphere is more pronounced: water features and the $\rm NH_3$ window show stronger enhancements, with extended differences increasing by $\rm 40{\text -}80$ ppm, whereas $\rm CH_4$ and $\rm CO/CO_2$ exhibit a substantial reduction in model differences.

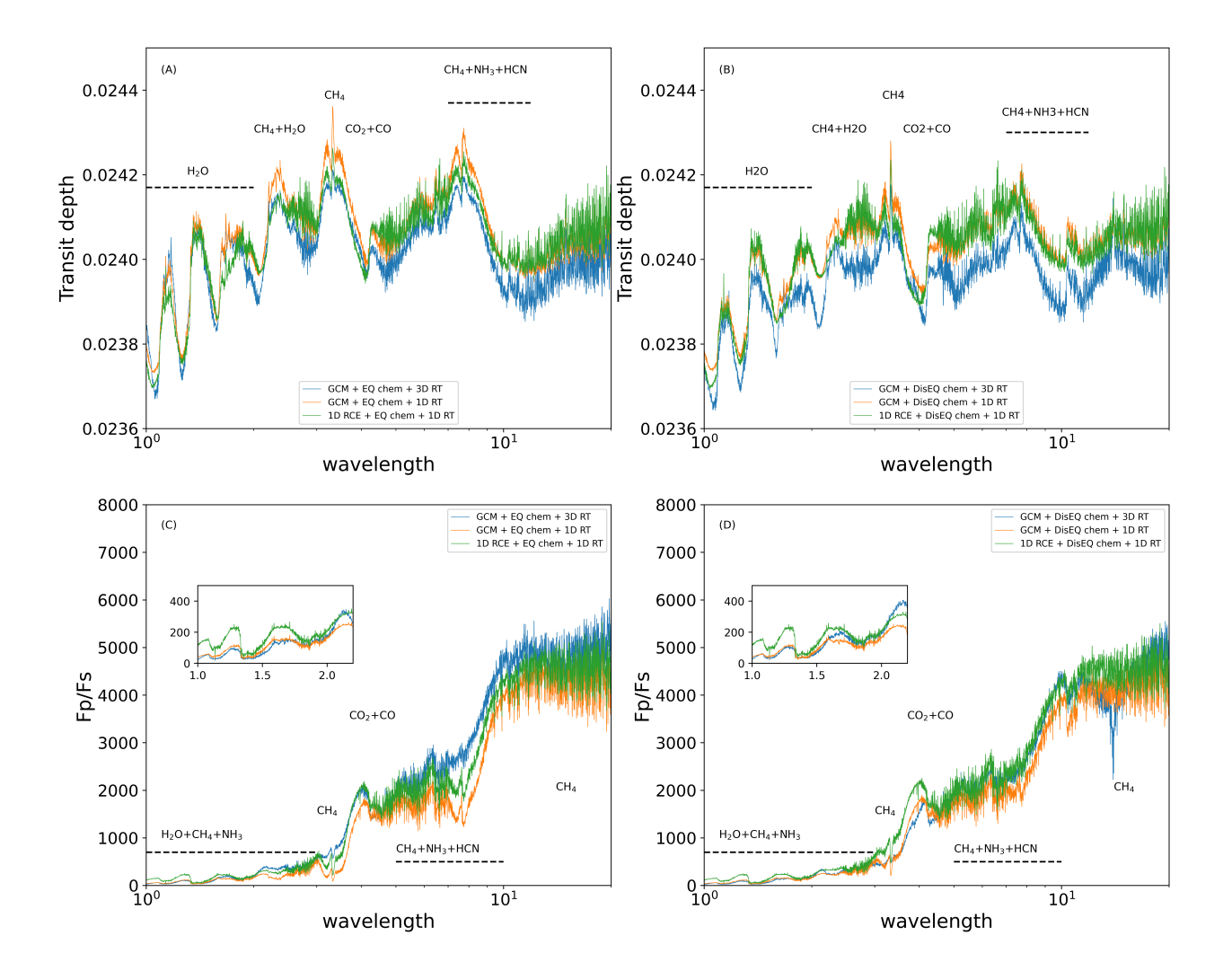


Figure 11. Subfigures (A) and (B) show the transmission spectra obtained using equilibrium and disequilibrium chemistry, respectively, while Subfigures (C) and (D) present the corresponding emission spectra for equilibrium and disequilibrium chemistry, computed using the T–P profiles shown in Figure 6. The color scheme follows that of (A) and (B), comparing the extended 1D RCE + 1D RT and 3D GCM + 1D RT spectra against the non-extended 3D GCM + 3D RT spectra for reference. Due to the limitation described in Section 3.5.4, the full 3D GCM + 3D RT configuration is not available for the extended setup.

3.5.6 Emission Spectra

In emission, the extended 1D–3D comparison shows that the largest spectral differences occur in the CH_4 , CO/CO_2 , and NH_3 bands, while H_2O features exhibit comparatively smaller variations. Under disequilibrium chemistry, extending the atmosphere enhances the contrast in CH_4 and CO/CO_2 regions by several hundred ppm. In contrast, H_2O bands vary only modestly, typically within 20–40 ppm, indicating limited sensitivity in the near-infrared features.

In the equilibrium case, the overall behavior remains similar but with smaller enhancements in the CH₄ and CO/CO₂ features and slightly larger increases in the H₂O and NH₃ windows. These results suggest that disequilibrium chemistry amplifies wavelength-dependent contrasts between the 1D and 3D frameworks in the ex-

tended cases, whereas equilibrium chemistry produces a more uniform offset across most bands, except for CH₄ and NH₃.

3.6 Noise simulation and Signal-to-Noise ratio

We used our models to generate noise simulations and computed the signal-to-noise ratio (SNR) for the differences between the spectra of the non-extended and extended cases, as shown in Table 6. These SNRs were evaluated over all wavelengths for observations consisting of three transits. Additionally, we calculated the SNR for one and five transits, as shown in Figure 12, where error bars for the non-extended cases are included for illustration.

To better understand variations in the major spectral features aris-

Table 6. This table presents SNR data for four cases: transmission and emission spectra in both equilibrium and disequilibrium conditions. The first two columns represent the wavelength region of the eight major spectral features and the corresponding molecule. Columns 3 and 4 show the signal strength in the 1D and 3D models (transit depth minus baseline transit depth / emission flux). Columns 5 and 6 present the absolute difference between these values and the SNR achieved with three transits of observation. In the non-extended cases, the "Difference (Non-extended)" column represents the difference between the full 1D RCE + 1D chemistry + 1D radiative transfer model and the 3D GCM + 1D chemistry + 3D radiative transfer model, whereas "Difference (Extended)" represents the difference between 1D RCE + 1D chemistry + 1D radiative transfer model (extended) and the 3D GCM + 1D chemistry + 3D radiative transfer model (non extended). The SNR for the extended cases is given in brackets next to the original SNR values, which correspond to the non-extended cases.

Transmission	Transmission Spectra (Disequilibrium Chemistry)						
Molecule	Wavelength (µm)	1D Signal	3D Signal	Difference	Difference	SNR	
	$(\mu \mathrm{m})$	(ppm)	(ppm)	(Non-extended, ppm)	(Extended, ppm)	(3 Transits)	
H ₂ O	1.1-1.35	294 (148)	222	72	74	5.95 (6.11)	
H_2O	1.35-1.6	384 (342)	303	81	39	4.25 (2.05)	
H_2O	1.7-2.25	270 (261)	161	109	100	5.32 (4.88)	
$H_2O + CH_4$	2.15-3	514 (488)	364	150	124	7.04 (5.82)	
CH_4	3.32	577 (535)	491	88	44	3.30 (1.65)	
$CO + CO_2$	3.7-5.1	401 (210)	276	125	66	5.07 (2.68)	
CH_4	7.4-7.74	564 (448)	464	100	16	3.15 (0.50)	
NH_3	9.86-12	405 (345)	280	125	65	1.66 (0.87)	

Transmission Spectra (Equilibrium Chemistry)						
Molecule	Wavelength (µm)	1D Signal	3D Signal	Difference	Difference	SNR
	(μm)	(ppm)	(ppm)	(Non-extended, ppm)	(Extended, ppm)	(3 Transits)
H ₂ O	1.1-1.35	237 (186)	330	93	144	6.10 (9.45)
H_2O	1.35-1.6	207 (202)	147	60	55	6.21 (5.69)
H_2O	1.7-2.25	310 (274)	207	103	67	5.70 (3.71)
$H_2O + CH_4$	2.15-3	520 (494)	383	137	111	7.68 (6.22)
CH_4	3.32	599 (563)	509	90	54	3.17 (1.90)
$CO + CO_2$	3.7-5.1	461 (375)	323	138	52	7.03 (2.65)
CH_4	7.4-7.74	601 (555)	494	107	61	2.55 (1.45)
NH_3	9.86-12	274 (341)	153	121	188	2.04 (3.17)

Emission Spectra (Disequilibrium Chemistry)						
Molecule	Wavelength (µm)	1D Signal	3D Signal	Difference	Difference	SNR
	$(\mu \mathrm{m})$	(ppm)	(ppm)	(Non-extended, ppm)	(Extended, ppm)	(3 Transits)
H ₂ O	1.1-1.35	253 (233)	105	148	128	14.08 (12.18)
H_2O	1.35-1.6	249 (243)	131	118	112	7.11 (6.75)
H_2O	1.7-2.25	258 (336)	172	86	164	7.92 (15.10)
$H_2O + CH_4$	2.15-3	645 (638)	424	221	214	8.30 (8.03)
CH_4	3.32	216 (1004)	501	285	503	16.12 (28.46)
$CO + CO_2$	3.7-5.1	1945 (2082)	1200	545	882	15.98 (25.87)
CH ₄	7.4-7.74	1865 (2759)	2552	687	207	36.93 (11.13)
NH_3	9.86-12	4850 (4762)	4043	807	719	12.77 (11.38)

Molecule	Wavelength (µm)	1D Signal				
Wioiccuic		i D Gigilai	3D Signal	Difference	Difference	SNR
	(μm)	(ppm)	(ppm)	(Non-extended, ppm)	(Extended, ppm)	(3 Transits)
H ₂ O	1.1-1.35	239 (238)	103	136	135	15.43 (15.31)
H_2O	1.35-1.6	204 (201)	117	87	84	9.80 (9.46)
H_2O	1.7-2.25	267 (266)	379	112	113	5.90 (5.95)
$H_2O + CH_4$	2.15-3	251 (270)	259	108	11	10.54 (1.07)
CH_4	3.32	297 (217)	668	371	451	12.41 (15.08)
$CO + CO_2$	3.7-5.1	1983 (1953)	1541	442	412	34.52 (32.15)
CH ₄	7.4-7.74	1865 (1889)	2868	1004	979	23.35 (22.77)
NH ₃	9.86-12	4884 (3794)	5485	601	1691	8.01 (22.53)

ing from different opacity sources, we identified eight key features in the 1–12 μm range. These correspond to the following wavelength intervals and associated molecular contributions: 1.1–1.35 μm (H₂O), 1.35–1.6 μm (H₂O), 1.7–2.25 μm (H₂O), 2.15–3 μm (H₂O + CH₄), 3.32 μm (CH₄), 3.7–5.1 μm (CO + CO₂), 7.4–7.74 μm (CH₄), and 9.86–12 μm (NH₃).

Figure 12 (A) shows the achieved signal-to-noise ratio (SNR) as a function of wavelength for transmission under equilibrium chemistry. The SNR calculations indicate that H_2O (SNR = 5.7–7.68), CO_2 ,

and CO (SNR = 7.03) are the molecules capable of distinguishing between the 1D and 3D models, with an SNR greater than 5 in three transits (Table 6). The figure also shows that increasing the number of observations from 3 to 5 transits enhances the detectability of CH₄, making it an important distinguishing marker.

As anticipated from the differences between the 1D and 3D models discussed in Section 3.5.2, we observe a decrease in SNR for disequilibrium chemistry, except for CH₄, as shown in Figure 12 (B). Additionally, we find that SNR increases as signal strength de-

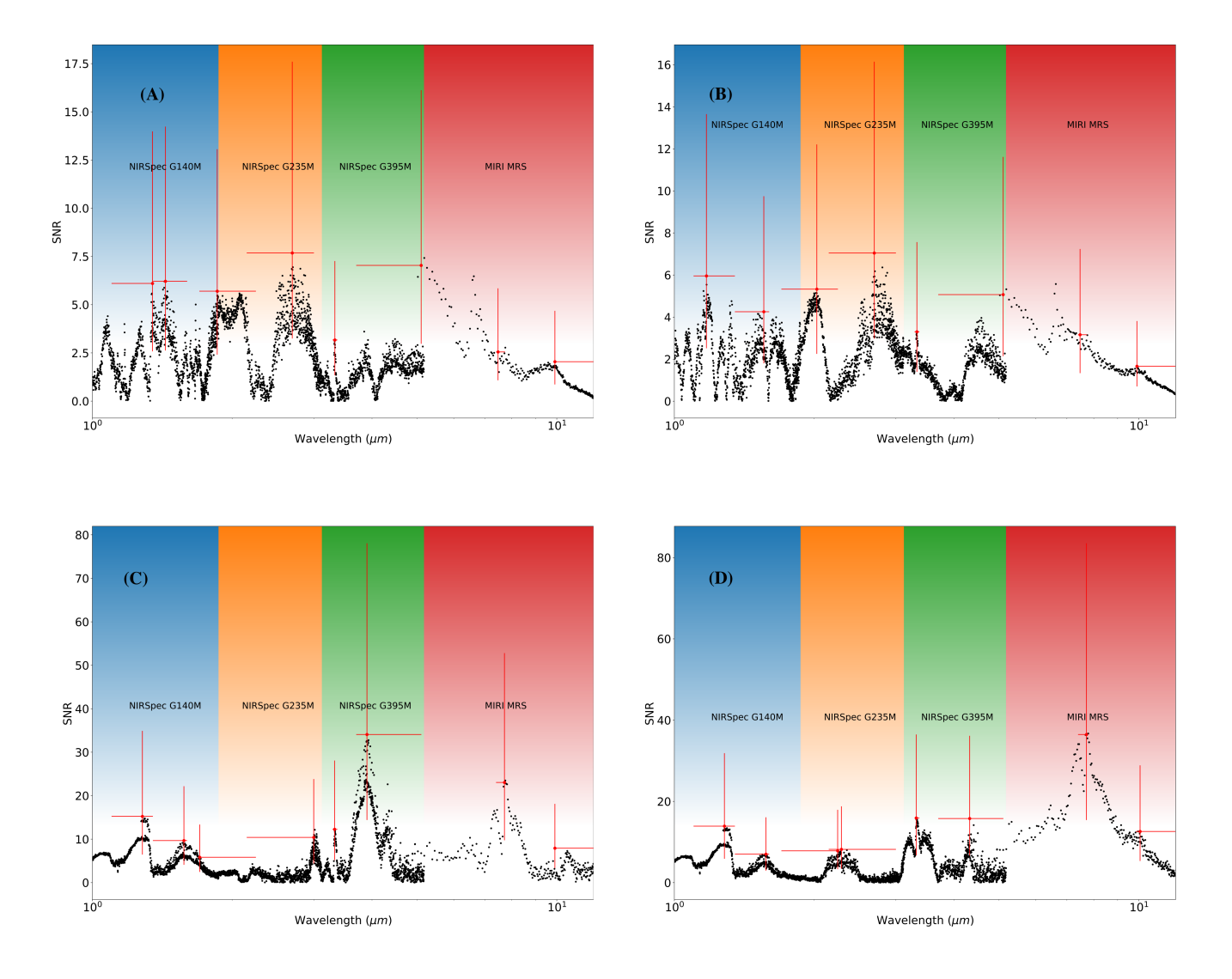


Figure 12. The black dotted curve shows the SNR for the differences between the 1D and 3D models over three transits for the non-extended cases, as listed in Table 6. The red scatter plot shows the SNR achieved over three transits for the eight major features shown in Table 6, with upper and lower error bars corresponding to five and one transits, respectively. The figure represents four cases of simulation: transmission with equilibrium chemistry (A), transmission with disequilibrium chemistry (B), emission with equilibrium chemistry (C), and emission with disequilibrium chemistry (D).

creases for the same NIRSpec G140M grism. This trend arises due to the wavelength-dependent efficiency of the grism, defined by its response function. For example, the NIRSpec G140M grism covers the 0.97–1.89 μm range, with peak efficiency around 1.2 μm .

A similar analysis for the equilibrium emission spectrum is shown in Figure 12 (C). The SNR achieved in distinguishing the 1D and 3D (DA) models in three transits of emission is more than twice that obtained for transmission. Unlike the transmission spectra, we find that CH₄ (SNR = 12.41–23.35), along with H₂O (SNR = 5.9–15.43), CO₂, and CO (SNR = 34.52), can also serve as key tracers for differentiating between the 1D and 3D models. For the emission spectrum under disequilibrium chemistry, our analysis reveals trends similar to those observed between equilibrium and disequilibrium transmission spectra.

A combined analysis highlights the 3.7–5.1 μ m feature, attributed

to CO and CO_2 , as the most critical spectral region for distinguishing between 1D and 3D models in all cases examined. Additionally, we identify case-specific distinguishing features: H_2O for transmission spectra and CH_4 for emission spectra, both of which provide insights into the planet's three-dimensional atmospheric structure.

We repeated the comparison using the extended atmospheric spectra (Fig. 11) and Table 6. In transmission, extending the 1D model leads to moderate but structured variations in SNR across wavelengths and chemical regimes. Under disequilibrium chemistry, most bands show a decrease in SNR, with reductions of nearly 50% in the CH₄ (3.3 μ m) and CO/CO₂ (3.7–5.1 μ m) regions, and smaller declines of 10–30% in the H₂O bands. Despite these reductions, the H₂O and blended H₂O+CH₄ regions remain the strongest contributors, retaining SNR values above 5 even after extension. In contrast, equilibrium chemistry shows the opposite trend: SNRs increase in the

long-wavelength H_2O and NH_3 windows by up to a factor of 1.5, reflecting the enhanced sensitivity of these bands to upper-atmosphere temperature gradients. CH_4 and CO/CO_2 features show moderate decreases in the extended case, indicating that the radiative structure of the lower atmosphere dominates their contribution. Overall, extending the model redistributes SNR between the near- and mid-infrared but preserves the hierarchy of dominant features, with equilibrium chemistry amplifying long-wavelength contrasts and disequilibrium chemistry reducing them.

In emission, the extended models show a wider range of SNR variations. Under disequilibrium chemistry, the CH₄ (3.3 μ m) and CO/CO₂ (3.7–5.1 μ m) bands show the largest SNR increases, by roughly 70–90% relative to the non-extended case, while H₂O features near 1–2 μ m change only slightly, remaining within 10–15%. At longer wavelengths, NH₃ (9.9–12 μ m) shows a small SNR decrease. Under equilibrium chemistry, SNR variations are more balanced: CH₄ and CO/CO₂ remain strong (SNR ~30–40) but decrease slightly, while NH₃ and H₂O bands show modest enhancements.

4 SUMMARY AND CONCLUSION

We modeled the atmosphere of HD 189733b to quantify the differences between 1D and 3D models, analyzing the required observational time to distinguish between these models and understand the 3D features of this planet. Our key findings and conclusions are summarized below:

- Our GCM models suggest inefficient heat redistribution in the dense lower atmosphere, resulting in homogeneous temperatures, while high wind velocities in the upper atmosphere drive efficient heat transport, creating notable variations. An eastward hotspot shift of $16^{\circ} \pm 4^{\circ}$, consistent with Spitzer and HST observations, highlights the influence of atmospheric winds driven by planetary rotation.
- The terminator region and median dayside-averaged T-P profiles differ significantly from the 1D T-P profile, highlighting the critical need for 3D modeling over 1D modeling, as transmission and emission spectra are sensitive to these regions rather than median global averages.
- The comparison of molecular abundances between 3D GCM-derived terminator/dayside profiles and 1D radiative-convective equilibrium models reveals significant differences. While 1D models predict higher abundances for most gases, key species like HCN, NH₃, and CH₄ show marked discrepancies due to differences in reaction pathways and rates.
- Synthetic transmission and emission spectra modeled for the 1D and 3D cases with equilibrium and disequilibrium chemistry reveal notable differences in key opacity sources such as H₂O, CH₄, CO, CO₂, and NH₃, where the T–P profiles extend to higher-pressure regions (10⁻⁴ bar for 3D cases and 10⁻⁶ bar for 1D cases, defined as non-extended cases). In these cases, equilibrium models predict stronger CH₄ and H₂O features, whereas disequilibrium models show reduced transit depths due to photochemical effects. Differences in the emission spectra between the 1D and 3D models are wavelength-dependent, with the 3D models showing greater sensitivity to chemical processes, particularly in the CH₄ features.
- For the non-extended cases, key spectral features in the 1–12 μ m range, including H₂O, CO₂, CO, and CH₄, serve as primary markers for distinguishing between models, with SNR > 5 achieved in most instances over three transits under equilibrium chemistry. Emission spectra exhibit higher SNRs than transmission spectra, with CH₄ and the combined CO+CO₂ bands emerging as critical indicators. Although disequilibrium chemistry generally reduces SNR values,

CH₄ remains an exception. The $3.7–5.1~\mu m$ range, dominated by CO and CO₂, consistently emerges as the most significant region for model differentiation across all scenarios.

- For the non-extended cases, we show that an observation time of three transits, equivalent to 11.4 hours (5.4 hours for the transit and 6 hours for the baseline), is required to achieve an SNR > 5 in transmission, while approximately one transit, equivalent to 3.8 hours (1.8 hours for the transit and 2 hours for the baseline), is sufficient to reach the same SNR in emission. These results provide an indirect estimate of the minimum observational time needed to distinguish between 1D and 3D atmospheric models for hot, irradiated gaseous exoplanets such as HD 189733b.
- \bullet For the extended cases, where lower pressures up to 10^{-8} bar modify the SNR in a wavelength- and chemistry-dependent manner, the near-infrared CH₄ and CO/CO₂ emission features, along with the long-wavelength H₂O and NH₃ transmission bands, are enhanced under equilibrium chemistry. In contrast, disequilibrium chemistry reduces the overall contrast and smooths SNR variations across the spectrum.

ACKNOWLEDGMENT

L.M. acknowledges funding support from the DAE through the NISER project RNI 4011. We thank the anonymous referee for the constructive comments that helped improve the manuscript.

DATA AVAILABILITY

All the codes used in this study, such as FASTCHEM, VULCAN, THOR, HELIOS, petitRADTRANS, and gCMCRT, are publicly available. All simulated data created in this study will be shared upon reasonable request to the corresponding author.

REFERENCES

Asplund M., Grevesse N., Sauval A. J., Scott P., 2009, ARA&A, 47, 481 Barman T. S., Hauschildt P. H., Allard F., 2001, ApJ, 556, 885

Batalha N. E., et al., 2017, Publications of the Astronomical Society of the Pacific, 129, 064501

Batalha N. E., Marley M. S., Lewis N. K., Fortney J. J., 2019, ApJ, 878, 70 Boucher A., et al., 2021, The Astronomical Journal, 162, 233

Boyajian T., et al., 2014, Monthly Notices of the Royal Astronomical Society, 447, 846–857

Cabot S. H. C., Madhusudhan N., Hawker G. A., Gandhi S., 2019, MNRAS, 482, 4422

Deitrick R., Mendonça J. M., Schroffenegger U., Grimm S. L., Tsai S.-M., Heng K., 2020, The Astrophysical Journal Supplement Series, 248, 30

Deitrick R., Heng K., Schroffenegger U., Kitzmann D., Grimm S. L., Malik M., Mendonça J. M., Morris B. M., 2022, Monthly Notices of the Royal Astronomical Society, 512, 3759

Drummond B., Tremblin P., Baraffe I., Amundsen D. S., Mayne N. J., Venot O., Goyal J., 2016, A&A, 594, A69

Drummond B., et al., 2020, A&A, 636, A68

Fauchez T. J., et al., 2022, The Planetary Science Journal, 3, 213

Fortney J. J., 2018, arXiv e-prints, p. arXiv:1804.08149

Fortney J. J., Barstow J. K., Madhusudhan N., 2021, in Madhusudhan N., ed., ExoFrontiers; Big Questions in Exoplanetary Science. pp 17–1, doi:10.1088/2514-3433/abfa8fch17

Fu G., et al., 2024, Hydrogen sulfide and metal-enriched atmosphere for a Jupiter-mass exoplanet (arXiv:2407.06163), https://arxiv.org/ abs/2407.06163 Goyal J. M., et al., 2018, MNRAS, 474, 5158

Grillmair C. J., et al., 2008, Nature, 456, 767

Guillot T., 2010, Astronomy & Astrophysics, 520, A27

Heng K., Showman A. P., 2015, Annual Review of Earth and Planetary Sciences, 43, 509

Inglis J., et al., 2024, ApJ, 973, L41

Innes H. I., Pierrehumbert R. T., 2022, in Bulletin of the American Astronomical Society. p. 102.210

JWST Transiting Exoplanet Community Early Release Science Team et al., 2023, Nature, 614, 649

Keles E., et al., 2019, Monthly Notices of the Royal Astronomical Society: Letters, 489, L37

Lee E. K. H., Parmentier V., Hammond M., Grimm S. L., Kitzmann D., Tan X., Tsai S.-M., Pierrehumbert R. T., 2021, MNRAS, 506, 2695

Lee E. K. H., et al., 2022, ApJ, 929, 180

Lee E. K. H., Tsai S.-M., Hammond M., Tan X., 2023, A&A, 672, A110

Lustig-Yaeger J., Meadows V. S., Lincowski A. P., 2019, AJ, 158, 27

Madhusudhan N., 2019, ARA&A, 57, 617

Madhusudhan N., 2024, arXiv e-prints, p. arXiv:2406.12794

Malik M., et al., 2017, AJ, 153, 56

Mayne N. J., et al., 2014, A&A, 561, A1

Mollière P., Wardenier J. P., van Boekel R., Henning T., Molaverdikhani K., Snellen I. A. G., 2019, A&A, 627, A67

Mukherjee S., Batalha N. E., Fortney J. J., Marley M. S., 2023, ApJ, 942, 71 Phillips M. W., et al., 2020, A&A, 637, A38

Pont F., Sing D. K., Gibson N. P., Aigrain S., Henry G., Husnoo N., 2013, Monthly Notices of the Royal Astronomical Society, 432, 2917

Quirino D., Gilli G., Navarro T., Turbet M., Fauchez T., Machado P., 2022, in EGU General Assembly Conference Abstracts. EGU General Assembly Conference Abstracts. pp EGU22–8185, doi:10.5194/egusphere-egu22-8185

Seager S., Deming D., 2010, ARA&A, 48, 631

Showman A. P., Fortney J. J., Lian Y., Marley M. S., Freedman R. S., Knutson H. A., Charbonneau D., 2009, The Astrophysical Journal, 699, 564

Steinrueck M. E., Koskinen T., Lavvas P., Parmentier V., Zieba S., Tan X., Zhang X., Kreidberg L., 2023, arXiv e-prints, p. arXiv:2305.09654

Stock J. W., Kitzmann D., Patzer A. B. C., 2022, MNRAS, 517, 4070

Tremblin P., Amundsen D. S., Mourier P., Baraffe I., Chabrier G., Drummond B., Homeier D., Venot O., 2015a, ApJ, 804, L17

Tremblin P., Amundsen D. S., Mourier P., Baraffe I., Chabrier G., Drummond B., Homeier D., Venot O., 2015b, ApJ, 804, L17

Tsai S.-M., Malik M., Kitzmann D., Lyons J. R., Fateev A., Lee E., Heng K., 2021, The Astrophysical Journal, 923, 264

Tsai S.-M., Moses J. I., Powell D., Lee E. K. H., 2023a, arXiv e-prints, p. arXiv:2305.19403

Tsai S.-M., Steinrueck M., Parmentier V., Lewis N., Pierrehumbert R., 2023b, MNRAS, 520, 3867

Wyttenbach A., Ehrenreich D., Lovis C., Udry S., Pepe F., 2015, A&A, 577,

Zamyatina M., et al., 2023, MNRAS, 519, 3129

Zhang M., Chachan Y., 2019, PLATON: PLanetary Atmospheric Transmission for Observer Noobs, Astrophysics Source Code Library, record ascl:1903.014 (ascl:1903.014)

de Kok, R.J. Brogi, M. Snellen, I.A.G. Birkby, J. Albrecht, S. de Mooij, E.J.W. 2013, A&A, 554, A82

de Wit, J. Gillon, M. Demory, B.-O. Seager, S. 2012, A & A, 548, A128

de Wit J., Gillon M., Demory B.-O., Seager S., 2012, Astronomy & Astrophysics, 548, A128